Renewable Energy 208 (2023) 240–250

Contents lists available at ScienceDirect

Renewable Energy

journal homepage: www.elsevier.com/locate/renene

Analysis on the thermal behaviour of the latent heat storage system using S-CO_2 and H-PCM

Ming Zhu [a], Wenguang Nan [a,*], Yueshe Wang [b]

[a] School of Mechanical and Power Engineering, Nanjing Tech University, Nanjing, 211816, China
[b] State Key Laboratory of Multiphase Flow in Power Engineering, Xi'an Jiaotong University, Xi'an, 710049, China

ARTICLE INFO

Keywords:
Thermal energy storage
Phase change
Natural convection
Melting
Solidification

ABSTRACT

Energy storage and utilization of CO_2 have attracted increasing attention due to international zero carbon plan. Here, the latent heat storage system using high-temperature phase change material (H-PCM) and supercritical CO_2 (S-CO_2) is analysed by using CFD simulation, in which the tube containing S-CO_2 is submerged in a tank containing the salt with high melting temperature. A new and combined phase transition model is developed to describe the dynamics of PCM in different phase state, and it is validated against experimental data in literature. The dynamics of natural convection is focused, and its effects on the heat storage system are analysed, including maximum natural convection velocity, phase interface, and melting pattern. The results show that natural convection has a great influence on the melting process of the H-PCM in the charging process. The melting pattern of H-PCM could be contrary between the cases with and without considering natural convection. During the discharging process, natural convection has little effect on the heat transfer of energy release due to its short duration. With the increase of ratio between the S-CO_2 tube and H-PCM tank, the strength of the natural convection of melting H-PCM is enhanced, especially the duration of natural convection.

1. Background

Carbon neutrality is an effective pathway to address environmental issues [1,2]. The world is accelerating the development of clean and renewable energy (i.e. solar energy, wind energy, hydro energy and geothermal energy, etc.) [3]. New energy would play an important role in this international carbon zero plan [4,5]. However, the current renewable energy sources, such as solar energy, usually suffer from a mismatch in timing or intensity between the energy supply and the energy demand [6,7], energy storage technology has attracted more and more attention [8], especially latent thermal energy storage [9–12] using phase change materials (PCM). The performance of latent thermal energy storage system often depends on the development of devices that provide encapsulation for phase change materials and heat transfer fluids, in which the ones using shell and tube are considered to be one of the most popular devices in commerce and industry [13–16], especially for large power plants. However, due to the complexity of phase change process of PCM, the dynamics of this kind of system has not been fully understood, especially for the ones with high-temperature, which is more attracted for power plants [17–20].

Although various work [21–26] has been done for latent thermal storage, there is only a few of work on the system with high temperature, where PCM usually has a melting point above 300 °C [27,28]. The heat transfer of latent heat storage system with high temperature and pressure using shell and tube could be analysed using effectiveness-number of transfer units (ε-NTU) [21,22] and logarithmic mean temperature difference (LMTD) [26]. For example, Pirasaci et al. [21] proposed a design model for storage unit based on ε-NTU, where the heat transfer energy efficiency between water/steam and PCM was also calculated. However, the phase transition process is usually simplified in these methods, for example, the natural convection phenomenon of melting PCM is ignored. Nowadays, as a supplement of experiment method, Computational Fluid Dynamics (CFD) has attracted more and more attention for the analysis of the dynamics of latent heat storage system [29–35]. Kadivar et al. [29] studied the eccentric double-pipe heat exchanger using the PCM with a melting point of 309.15 °C, where several geometrical configurations were explored. Their results showed that the eccentric-annulus configuration ($r^* = 0.841$ and $\Theta = 0.029\pi$) performed best. Riahi et al. [31] investigated the performance of a shell and tube heat exchanger, where the sodium nitrate with a melting temperature of 306.8 °C was used as the PCM. Their results showed that horizontal counter flow and parallel flow configurations showed on

* Corresponding author.
E-mail address: nanwg@njtech.edu.cn (W. Nan).

https://doi.org/10.1016/j.renene.2023.03.041
Received 11 December 2022; Received in revised form 4 March 2023; Accepted 8 March 2023
Available online 13 March 2023

average 10% higher effectiveness for the charging process than that of the vertical configurations. Tiari et al. [34] simulated the charging process of a finned heat pipe-assisted LHTES system using the PCM with a melting point of 608 °C, and their results showed that natural convection had considerable effects on the melting process of the PCM. Prasad et al. [35] used effective heat capacity method to analyse the melting and solidification process in shell and tube cascade LHTES, in which the melting point of PCMs were all over 570 °C. Their results showed that the inlet temperature of HTF played a major role in decreasing the charging/discharging time. However, the mechanisms and details of the dynamics of melting PCM need further analysis, such as natural convection and melting pattern.

In recent years, with the development of concentrated solar thermal power generation technology and international zero carbon plan [36–38], CO_2 has attracted an increasing attention in engineering as a heat transfer fluid (HTF). Supercritical CO_2 (S-CO_2) has the advantages of a wide range of sources, excellent heat transfer characteristics [22,39]. At the same time, the cycle thermal efficiency of the S-CO_2 Brayton cycle in the temperature range of 773–973 K is significantly higher than that of the steam power cycle in this temperature region. Therefore, S-CO_2 has the potential to be used as a high temperature heat transfer fluid in concentrated solar thermal power plants [40,41]. Liu et al. [42] compared the solar power generation system using S-CO_2 with the traditional power generation system using water (steam), and the results showed that the solar energy conversion efficiency was significantly improved by S-CO_2. According to China "carbon peak" and "carbon neutrality" goals, the heat storage system using S-CO_2 attracts more and more attention from the power plant, especially the concentrated solar power (CSP). In power plant, the heat is usually in high temperature, resulting in the increase of the demand of the system using the PCM with high temperature melting point (H-PCM). However, the latent thermal storage system using the combination of H-PCM and S-CO_2 has not been explored in detail so far.

This work focuses on the heat transfer process between S-CO_2 and H-PCM in the latent heat storage system, in which the tube containing S-CO_2 is submerged in a tank containing H-PCM. A novel phase transition flow model is developed to describe the dynamic behaviour of PCM in different states, and validated against data in the literature. The dynamics of natural convection is focused and its effect on the heat storage system is analysed, where several factors are considered, including initial temperature difference and the size ratio between S-CO_2 tube and H-PCM tank. This provides a step forward in our understanding of the natural convection of melting PCM, which is a key factor affecting the heat transfer process in latent thermal storage system using H-PCM and S-CO_2.

2. Numerical model

Two kinds of materials are involved in this work: S-CO_2 for energy exchange, and H-PCM for energy storage. For the former, the flow dynamics and heat transfer could be described by traditional Navier-Stokes and energy equations, which are not shown here for simplicity. For the latter, different states could be involved during energy charging/discharging processes, i.e. solid, liquid, and a mixture of solid and liquid, making the flow dynamics and heat transfer complex. Here, the governing equations of PCM are described below, where a combined phase transition model is developed in COMSOL Multiphysics software and validated against experimental data.

2.1. Governing equations

The governing equations for PCM are shown below, including continuity equation, momentum equation and energy equation [43,44]:

Continuity Equation:

$$\nabla \cdot \boldsymbol{u} = 0 \tag{1}$$

Momentum equation:

$$\rho \frac{\partial \boldsymbol{u}}{\partial t} + \rho(\boldsymbol{u} \cdot \nabla)\boldsymbol{u} = -\nabla p + \mu \nabla^2 \boldsymbol{u} + \boldsymbol{S}_m + \boldsymbol{S}_b \tag{2}$$

Energy equation:

$$\frac{\partial(\rho H)}{\partial t} + \rho \nabla \cdot (H\boldsymbol{u}) = \nabla \cdot (k \nabla T) \tag{3}$$

where ρ is the density; $\boldsymbol{u}$ is the velocity vector; k is the thermal conductivity; p is the pressure; μ is the dynamic viscosity, depending on liquid fraction, as described in Section 2.2; $\boldsymbol{S}_m$ and $\boldsymbol{S}_b$ are the source terms in the momentum equation, respectively, as described in Section 2.2. H is the enthalpy of PCM.

$$H = c_p T + \Delta H \tag{4}$$

where c_p is the specific heat of the PCM; ΔH is the modified latent heat added to the enthalpy in cells with melting PCM.

2.2. Phase transition model

A major difficulty in analysing melting-solidification systems using the fixed grid method is the mass and heat transfer around the phase transition. The basic approach to overcome this problem is using the enthalpy-porosity method. Based on the work of Rösler et al. [45,46] and Voller et al. [47], a combined method is developed here:

1) Considering the variation of heat transfer with liquid fraction of PCM, ΔH is defined as:

$$\Delta H = sL \tag{5}$$

where L is the latent heat of PCM; s is the liquid fraction, and it is calculated by an error function:

$$s = 0.5 \,\mathrm{erf}\left(4.0\left(\frac{T - T_m}{T_l - T_s}\right)\right) + 0.5 \tag{6}$$

where $T_m = (T_l + T_s)/2.0$ is the melting temperature, while T_l and T_s are the liquidous and solidus temperature, respectively. Compared to traditional linear model (as shown in Eq. (7)) with Ben et al. [48], the liquid fraction given in Eq. (6) is smoother at the transition point between melting and solidification, as shown in Fig. 1.

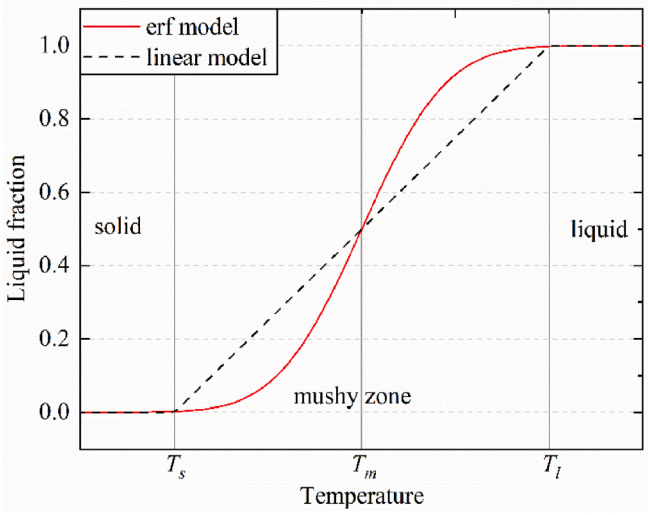

Fig. 1. Comparison of the calculation of liquid fraction between different models.

$$s=\begin{cases}0 & T\le T_s\\ \dfrac{T-T_s}{T_l-T_s} & T_s<T<T_l\\ 1 & T\ge T_l\end{cases} \tag{7}$$

2) Considering the interaction force between the liquid phase and solid phase in the mushy zone, an appropriate source term $\boldsymbol{S}_m$ is implemented into the momentum equation. Based on the Carman-Kozeny equations for flow in porous media, as previously studied by Voller and Prakash [47], $\boldsymbol{S}_m$ in Eq. (2) is given as:

$$\boldsymbol{S}_m = A\boldsymbol{u} \tag{8}$$

$$A = -C\frac{(1-s)^2}{s^3+b} \tag{9}$$

where A is the porosity function; C is a large constant related to the permeability of porous media, which is given as $C=10^5$ in this work; b is a small numerical constant (i.e. 0.001), which is used to avoid zero being divided in Eq. (9) in the solid phase. In the liquid phase ($s=1$), the porosity function A is zero, and the momentum equation is reduced into the form of one-phase fluid flow. In the solid phase ($s=0$), the porosity function A is very large (i.e. C/b), and the velocity of PCM calculated from governing equations would diminish to zero, corresponding the reality of solid. In the mushy zone, the porosity function A decreases with the liquid fraction, and the momentum equation is in the same form as Darcy law.

3) The viscosity μ is a function of the liquid fraction, and it can be linked to temperature, given as:

$$\mu = \mu_l \cdot s + C\mu_l \cdot (1-s) \tag{10}$$

where μ_l is the viscosity of PCM in full liquid phase ($s=1$); C is a large constant, which is assumed to be the same value in Eq. (9) for simplicity. Thus, the viscosity changes from a finite value in full liquid phase ($s=1$) to a very large value in full solid phase ($s=0$), as shown in Fig. 2.

4) The source term $\boldsymbol{S}_b$ in the momentum conservation equation (as shown in Eq. (11)) is the buoyancy source term using Boussinesq approximation:

$$\boldsymbol{S}_b = \rho \boldsymbol{g}\beta\left(T-T_{ref}\right) \tag{11}$$

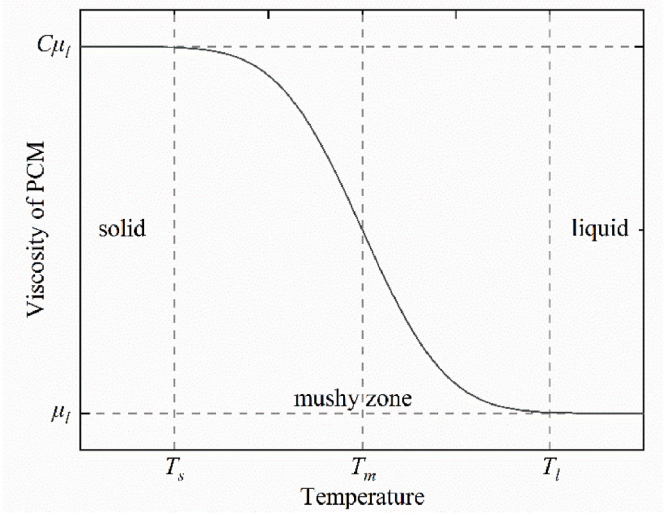

Fig. 2. Variation of viscosity of PCM with temperature.

where β is the thermal expansion coefficient, which is assumed to be linear to liquid fraction:

$$\beta = \beta_l \cdot s \tag{12}$$

where β_l is thermal expansion coefficient in full liquid state.

2.3. Model validation

The phase transition model described above is implemented into COMSOL Multiphysics software. It is validated by comparing the simulation results with the experiment of Gau & Viskanta [49], where gallium is melted in a cavity, as shown in Fig. 3. The cavity has a length of 88.9 mm in X direction and a height of 63.6 mm in Y direction. In the cavity, the left and right sides are the hot wall ($T_{hot}=311.15$ K) and cold wall ($T_{cold}=301.45$ K), respectively, while the upper and lower walls are adiabatic. The initial temperature of gallium in the cavity is specified as the same as the cold wall. The physical properties of gallium are shown in Table 1.

The phase interface obtained in this work is compared with the experimental data of Gau & Viskanta [49], and the simulation result (linear model) of Brent et al. [50] is also included, as shown in Fig. 4. The results show that the melting process develops faster in the upper part of the cavity, which is mainly due to natural convection. The liquid gallium heated by the hot wall would move upward, and then is cooled down when contacting with the front side of the mushy region, afterwards, it moves downwards and is reheated by the left wall. It can be found that the results in this work agree well with Gau & Viskanta [49] and Brent et al. [50]. There is a small deviation between the numerical results (both this work and Brent et al. [50]) and the experiment work. It may be due to the anisotropic thermal conductivity within gallium and three-dimensional effects in the experimental setup. Compared to the work of Brent et al. [50], the results using the combined model developed in this work agree better with the experimental data.

In addition, the combined phase transition model is further validated by comparing the results with the experimental work of Trp [51], where a thermal energy storage system is used. In the experiment, an HTF pipe (0.033 m in diameter) is embedded in a cylindrical container (0.128 m in diameter) filled with PCM. The PCM is an industrial-grade paraffin with an initial temperature of 20 °C. The HTF is water, with an inlet temperature of 45 °C and flow rate of 0.017 kg/s. To speed up the simulation, a two-dimensional axisymmetric model is used in the simulation. The temperature change at the $r=0.0265$ m, $Z=0.35$ m (position 5 in the Trip experiment) is monitored by using the probe tool. As shown in Fig. 5, the simulation results using the combined model developed in this work are in good agreement with the experimental data, and the maximum temperature difference is only within 1.5 K.

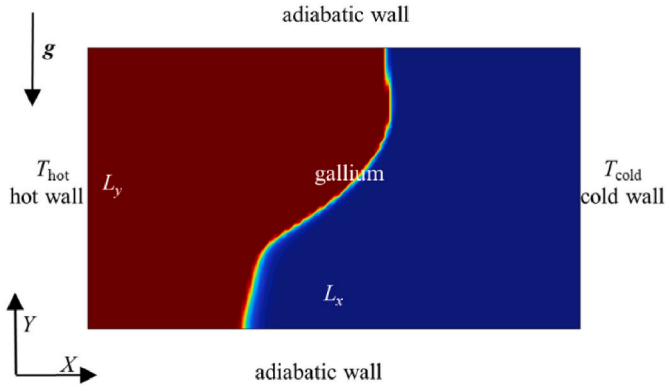

Fig. 3. Boundary conditions of the cavity in the experiment of Gau and Viskanta (1986).

Table 1
Physical properties of gallium.

Parameters	Value
Density, ρ (kg/m^3)	6093
Thermal Expansion Coefficient, β_l (1/K)	1.2×10^{-4}
Thermal Conductivity, k (W/(m·K))	32.0
Latent heat of fusion, L (J/kg)	80,160
Specific heat capacity, C_p (J/(kg·K))	381.5
Dynamic viscosity, μ_l (kg/(m·s))	1.81×10^{-3}
Solidus temperature, T_s (K)	302.93
Liquidous temperature, T_l (K)	303.43

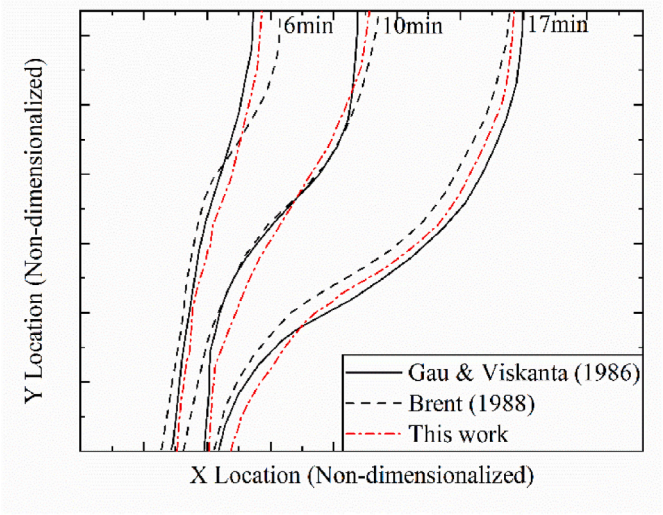

Fig. 4. Comparing of phase interface curves between this work and the data in the experiment of Gau & Viskanta (1986) and simulation of Brent (1988).

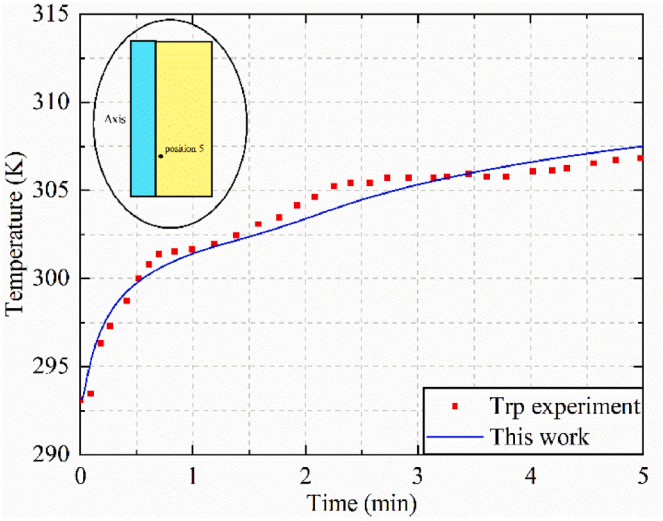

Fig. 5. Comparison of the simulation results using the combined model developed in this work against with the experimental data of Trp (2005).

2.4. Simulation conditions

The heat storage system used in this work is shown in Fig. 6, in which several tubes containing S-CO_2 are submerged in a tank containing H-PCM (58% NaCl + 42% $MgCl_2$) [33]. Their physical properties are summarised in Table 2, where the value for H-PCM is extracted from Li et al. [52], Toerklep et al. [53] and Takeda et al. [54], while the value for S-CO_2 is obtained from NIST REFPROP database. Due to the periodicity

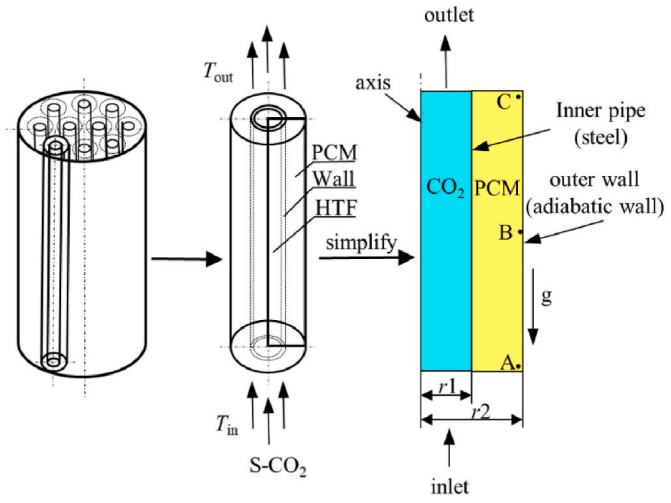

Fig. 6. Schematic diagram of latent thermal storage system, where axial symmetry model is used in the simulation.

Table 2
Physical properties of H-PCM and S-CO_2.

Parameters	H-PCM	S-CO_2
Density, ρ (kg/m^3)	2227	$0.0007T^2$-$1.1488T$ + 595.59
Thermal Expansion Coefficient, β_l (1/K)	2.7×10^{-4}	–
Thermal Conductivity, k (W/(m·K))	0.95	$2 \times 10^{-8}T^2$+$4 \times 10^{-5}T$+0.016
Latent heat of fusion, L (J/kg)	316,000	–
Specific heat capacity, C_p (J/(kg·K))	1000	1245.9
Dynamic viscosity, μ_l (kg/(m·s))	4.1×10^{-3}	$7 \times 10^{-12}T^2$+$2 \times 10^{-8}T$+2×10^{-5}
Solidus temperature, T_s (K)	822	–
Liquidous temperature, T_l (K)	830	–

of the tube array in the tank, the system is simplified to an individual inner tube (S-CO_2) immersed in a long tank (H-PCM), where the axial symmetry model is used, and the upper, lower and outer walls of H-PCM zone are assumed to be adiabatic, as shown in Fig. 6.

The heat transfer fluid is introduced into the system from the bottom, with pressure of 16.5 MPa, and mass flow rate of 0.0195 kg/s. The heat resistance between S-CO_2 and H-PCM due to tube thickness is also considered, where the material of steel is used, with thermal conductivity of 16.27 W/(m·K) and thickness of 2 mm. Both the heat charging process (i.e. H-PCM melting) and discharging process (i.e. H-PCM solidification) are simulated here. In the charging process, the inlet temperature of S-CO_2 is 873 K, and the initial temperature of solid H-PCM is 773 K. In the discharging process, both the latent and sensible heat of H-PCM is transferred to S-CO_2, with the inlet temperature of 473 K for S-CO_2, and the initial temperature of 873 K for H-PCM. The height of system is $H = 1000$ mm, while the radius of the tube and tank are $r_1 = 12.7$ mm and $r_2 = 25.4$ mm, respectively, if not specified. During the simulation, the temperature and liquid fraction of H-PCM are monitored at points A, B and C, as shown in Fig. 6. The radial position is $r_2 - r = 0.1$ mm for point A, B and C. The axial direction for points A, B and C are $z = 1$ mm, $z = H/2$ and $z = H - 1$ mm, respectively. The average temperature and liquid fraction of the entire H-PCM zone are also examined. In S-CO_2 zone, the temperature at the midpoint of the outlet is tracked. Prior to the analysis, the sensitivity of the simulation results to the grid size (i.e. 20 × 250, 40 × 500, 60 × 800 cells) is also examined, as shown in Appendix A, and 40 × 500 cells are used in the simulation for following analysis, if not specified, above which the results are not changed by finer cells.

3. Results and analysis

3.1. Natural convection

In this section, the charging process is considered, and two cases, i.e. with and without considering natural convection, are compared and analysed. In the latter, the buoyancy source term in Eq. (11) is set to zero.

Fig. 7 shows the variation of the contour of liquid fraction of H-PCM with time, where *X*-direction is zoomed in five times for easy observation. For the case without considering natural convection, as shown in Fig. 7 (a1-g1), heat is mainly transported by conduction. In the bottom section of H-PCM zone, as the temperature difference between S-CO_2 and H-PCM is larger than other positions, H-PCM melts faster. In the middle and upper sections of H-PCM zone, the interface of mushy zone is almost parallel to the left wall. For the case with considering natural convection, as shown in Fig. 7 (a2-g2), the melting process of H-PCM is much different to the case without considering natural convection. In the early stage of melting, as shown in Fig. 7 (a2), the heat transfer is mainly due to conduction, and the H-PCM is gradually melted in the same pattern as Fig. 7 (a1). In the middle stage of melting process, as shown in Fig. 7 (b2-d2), the melting of H-PCM at the bottom zone is slowed down, while the melting of H-PCM at the top zone is speeded up. Therefore, compared to the bottom zone, the top zone is much earlier fully melted, as shown in Fig. 7 (e2-g2). Therefore, natural convection significantly changes the melting dynamics of H-PCM. Natural convection accelerates the melting process at the top and stabilize the bottom at a constant temperature for a long time, while the melting extent of H-PCM decreases along the axial height when not considering the natural convection.

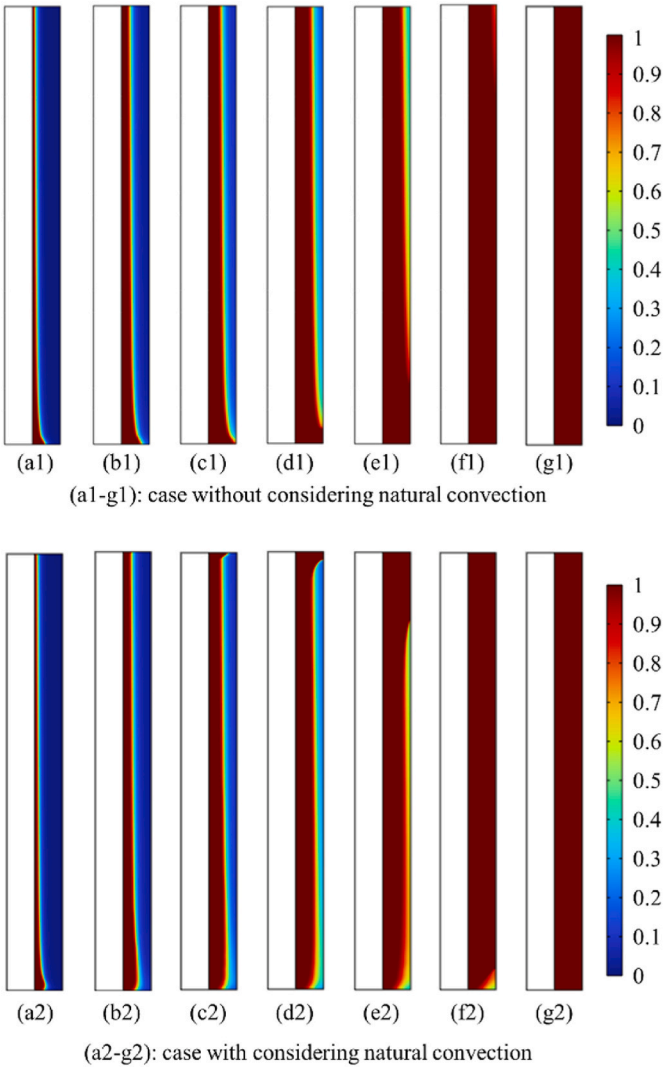

Fig. 7. Variation of the contours of liquid fraction of H-PCM with time, where the value of 0 indicates that all H-PCM is in solid state, and the value of 1 indicates that all H-PCM is in liquid state. The *X*-direction (i.e. horizontal direction) is zoomed in five times for easy observation, and a1 & a2: $t = 15$ min, b1 & b2: $t = 30$ min, c1 & c2: $t = 45$ min, d1 & d2: $t = 60$ min, e1 & e2: $t = 75$ min, f1 & f2: $t = 90$ min, g1 & g2: $t = 105$ min.

It is mainly due to the action of natural convection, as shown in Fig. 8. For the zone close to the inner wall, H-PCM has a higher temperature and moves upward, resulting in the transfer of heat from the bottom to upper section. Therefore, the melting degree of H-PCM is speed up at the top section while slowing down at the bottom section. Correspondingly, for zone far away from the inner wall, the melted H-PCM with lower temperature moves down under the driven of buoyancy force, resulting in further cooling of H-PCM at the bottom section. This leads to natural convection, which is also called thermosiphoning phenomenon.

Fig. 9 shows the total time used for fully melting of H-PCM at different sections. Here, the axial locations of bottom, middle and top sections correspond to $z = z_A$, $z = z_B$ and $z = z_C$, respectively, as shown in Fig. 6, and the radial locations of all sections are $r = r_1 \sim r_2$. For the case without considering natural convection, the total time increases with the axial height of the sections, which is intuitively expected, as the energy of S-CO_2 that could be stored decreases along the axial direction. However, this trend is contrary for the case considering natural convection. For example, the total time increases to about 2 times for the bottom section, while decreases to about half for the top section. This is caused by natural convection or thermosiphoning phenomenon, as discussed above.

Fig. 10 shows the position of the phase interface at bottom and top sections, where the position is the radial coordination *r* of the mesh cell with liquid fraction of 1, and it is further normalised by $(r - r_1)/(r_2 - r_1)$. Compared to the case not considering natural convection, in early stage, i.e. $t < 5$ min for bottom section and $t < 30$ min for top section, there is no much difference for the case considering natural convection, as the natural convection is not well established during this period. After this period, the natural convection plays an important role for the shift of the phase interface, e.g. the rate of movement of the phase interface moves much more quickly to the tank wall than the case without considering natural convection. It is interesting that the shift of the phase interface at

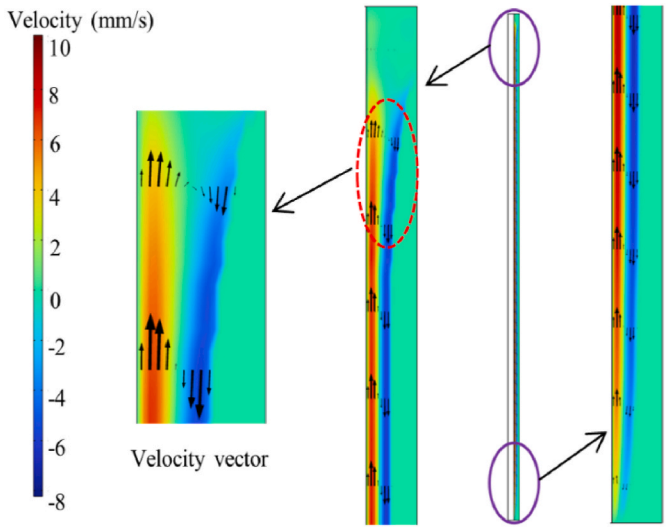

Fig. 8. Velocity vector of H-PCM at $t = 60$ min for the case considering natural convection, where the H-PCM is also coloured by velocity in *Z* direction.

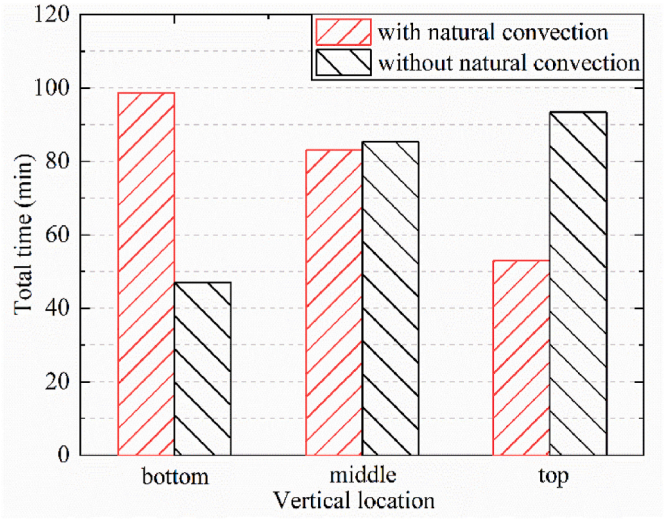

Fig. 9. Total time used for fully melting of H-PCM at different sections.

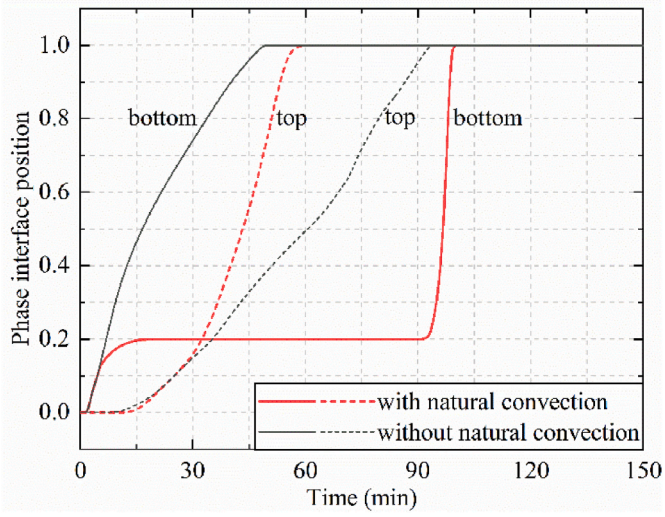

Fig. 10. Phase interface position at bottom and top sections, where the position is normalised by $(r - r_1)/(r_2 - r_1)$.

the bottom section is almost suspended during $t = 20$–90 min. This is due to that the heat from S-CO_2 is transferred to the upper part of H-PCM zone under the effect of thermosiphoning. It should be noted that once the phase interface at the bottom section begins to shift again, it would move very quickly to the wall of the H-PCM tank.

The melting pattern could also be indicated by the temperature shown in Fig. 11. Here, a non-dimensional number Θ is used to describe the deviation between local temperature T (i.e. at bottom and top part of H-PCM zone) and averaged value T_{ave}, given as:

$$\Theta = \frac{T - T_{ave}}{|T_{int,\mathrm{HTF}} - T_{int,\mathrm{PCM}}|} \tag{13}$$

where T_{int} is the initial temperature of the H-PCM or S-CO_2. For the bottom part, at most time, i.e. 30-120 min, Θ has a positive value for the case considering natural convection while it has a negative value for the case not considering natural convection, which is similar to the top part. Therefore, for the case not considering natural convection (dotted line in Fig. 11), the bottom has a larger temperature while the top has a smaller temperature, compared to the averaged value; for the case considering natural convection, it is in the opposite situation. It suggests that natural convection results in opposite evolution of local temperature at the

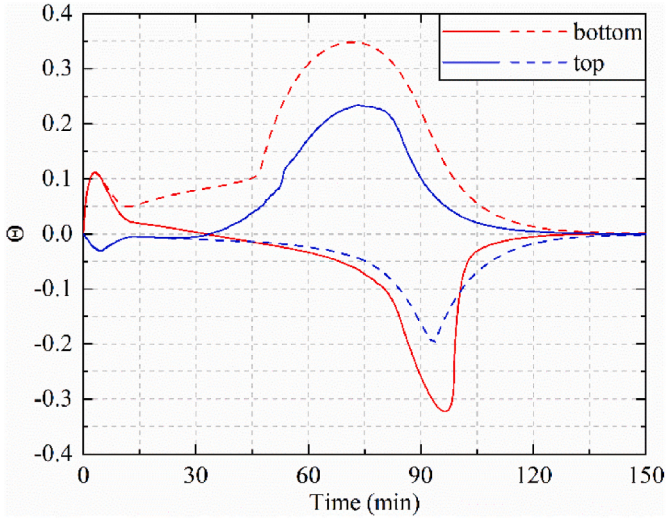

Fig. 11. Difference between local temperature and averaged value at bottom and top sections for the cases with considering natural convection (solid line) and not considering natural convection (dotted line).

bottom and top parts of H-PCM zone.

3.2. Effect of temperature difference

In this section, two kinds value of initial temperature difference between S-CO_2 and H-PCM is used, i.e. $\Delta T = 100$ K and 400 K. The effect of ΔT on both charging and discharging processes are analysed, where the cases with and without considering natural convection are compared.

In the discharging process, the phase interface of the H-PCM is shown in Fig. 12. Compared to the charging process in Fig. 7, natural convection has little effect on the evolution of phase interface of the H-PCM in the discharging process. In all cases shown in Fig. 12, the solidification of H-PCM is firstly finished at the bottom part, and finally at the top part. Thus, the phase transition pattern is the same in both the cases considering and not considering the natural convection. This is different from the charging process, where the natural convection could lead to

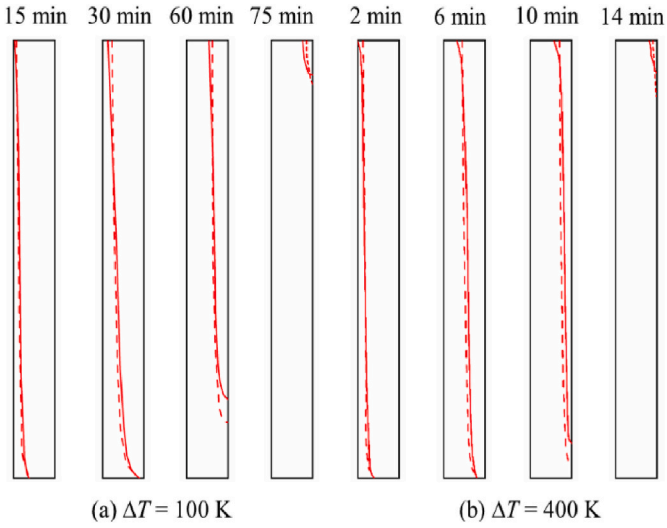

Fig. 12. Positions of the solidification phase interface for the cases with the initial temperature difference between S-CO_2 and H-PCM at (a) $\Delta T = 100$ K and (b) $\Delta T = 400$ K during discharging process, where the cases with (solid line) and without (dotted line) considering natural convection are compared, and X-direction (i.e. horizontal direction) is zoomed in five times for easy observation.

opposite phase transition pattern, compared to the case without considering natural convection. It is consistent with the local temperature shown in Fig. 13. It shows the temperature of top part is larger than the average value while the bottom part is less than the average value in both the cases with and without considering natural convection, which is much different to the ones shown in Fig. 11. After a short time (i.e. about 12 min), the effect of natural convection is minimal.

It should be noted that this phenomenon is mainly due to the duration of natural convection. It could be indicated from Fig. 14, where the maximum velocity of H-PCM is illustrated for the case considering natural convection. Compared to charging process, the velocity of H-PCM due to natural convection is much larger. For example, for ΔT = 100 K, the largest value is around 16 mm/s in Fig. 14(a) for charging process, while it could reach 41 mm/s in Fig. 14(b) for discharging process. However, it should be noted that the duration of natural convection is much shorter for discharging process. For example, for ΔT = 100 K, the velocity decreases quickly to zero within a time less than 12 min in Fig. 14(b) for discharging process, while it decreases to zero when the time is larger than 120 min in Fig. 14(a) for charging process. In discharging process, the natural convection only takes effect before solidification, i.e. from releasing sensible heat to the beginning of solidification, while in the charging process, the natural convection could take longer effect, i.e. from the beginning of melting to the end where H-PCM reaches the same temperature of S-CO_2.

Fig. 15 shows the variation of the heat stored or released by the system with time. In the charging process, for the case of ΔT = 100 K, the stored heat is about 1380 kJ, which is finished in about 120 min. As the initial temperature difference ΔT increases to 400 K, the stored heat increases, in which the increment (i.e. 1036 kJ) is mainly due to the sensible heat in the early stage of charging process. In the discharging process, for the case of ΔT = 400 K, the heat release rate of H-PCM is much faster, which is almost finished in 60 min. The time required for energy being fully charged during the charging process differs very little under different ΔT, while the time required for energy being fully released during the discharge process varies greatly under different ΔT. This is mainly due to the temperature difference between the initial temperature of the S-CO_2 and the phase transition temperature of the H-PCM.

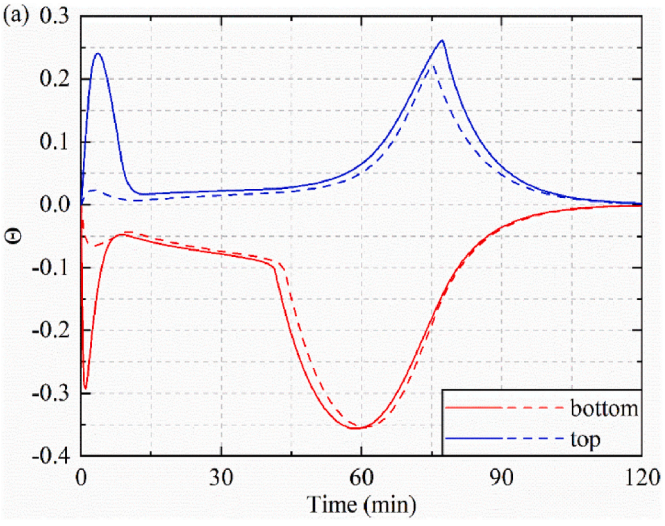

Fig. 13. Difference between local temperature and averaged value at bottom and top sections of H-PCM zone for the cases with considering natural convection (solid line) and not considering natural convection (dotted line) in discharging process with ΔT = 100 K.

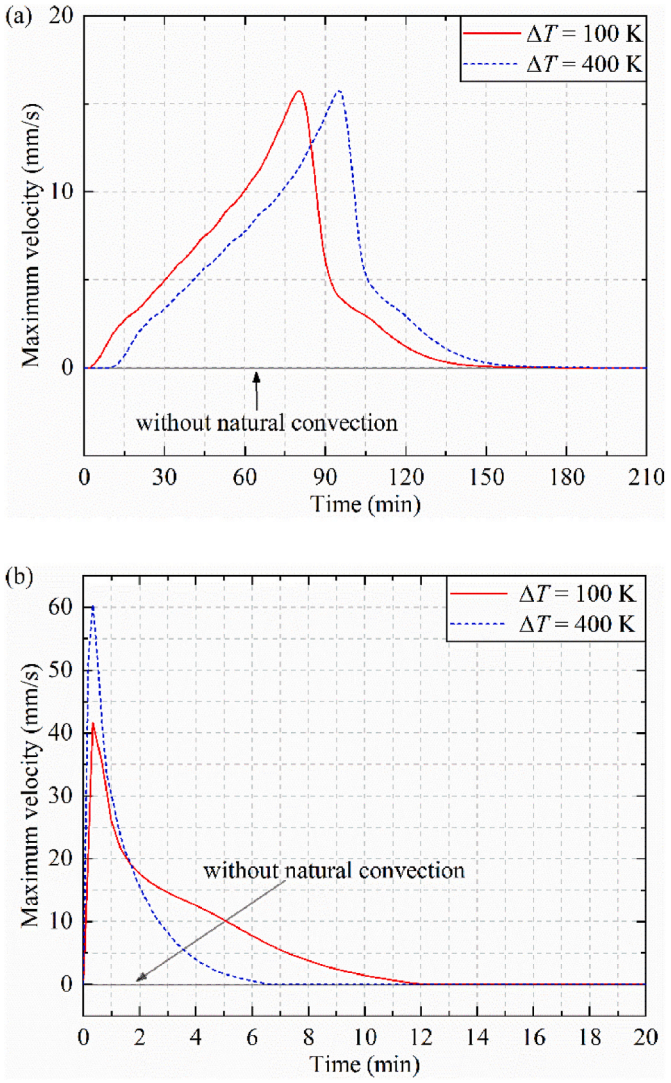

Fig. 14. Variation of maximum H-PCM velocity with time in (a) charging process and (b) discharging process, where natural convection is considered.

3.3. Effect of radius ratio

In this section, the effect of the pipe radius ratio on the heat transfer between H-PCM and S-CO_2 is investigated. Here, only charging process with considering natural convection is involved. The radius r_1 of S-CO_2 tube is unchanged while the radius r_2 of H-PCM tank is varied, and the non-dimensional parameter φ is defined in Eq. (14), where a larger value of φ indicates larger amount of H-PCM used in the tank. Beside the standard case (i.e. φ = 1) described in Section 3.1, another two values, i.e. φ = 0.5 and 2, are also used.

$$\varphi = \frac{r_2 - r_1}{r_1} \tag{14}$$

Fig. 16 shows the total time used for fully melting of H-PCM at different sections of H-PCM zone. With the increase of radius ratio φ, the time used to be completely melted for each section (i.e. bottom, middle, top) increases significantly. For the case of φ = 0.5, the bottom section is firstly fully melted while the middle and top sections take the same time to be fully melted. This is different to the case discussed in Section 3.1. It is mainly due to the duration of charging process is too short, and the natural convection does not have enough time to take effect. For the case of φ = 2, the bottom needs more time to be fully melted, than the sections of top and middle. With the increase of radius ratio, the difference

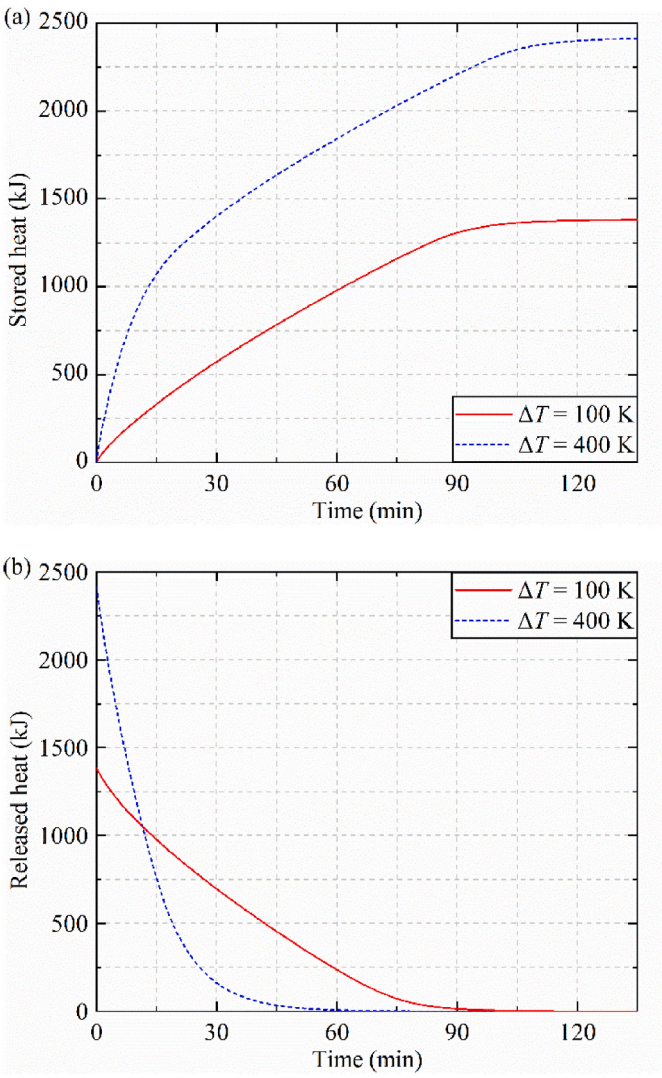

Fig. 15. Evolution of heat of H-PCM with time: (a) stored heat in the charging process; (b) released heat in the discharging process, where natural convection is considered.

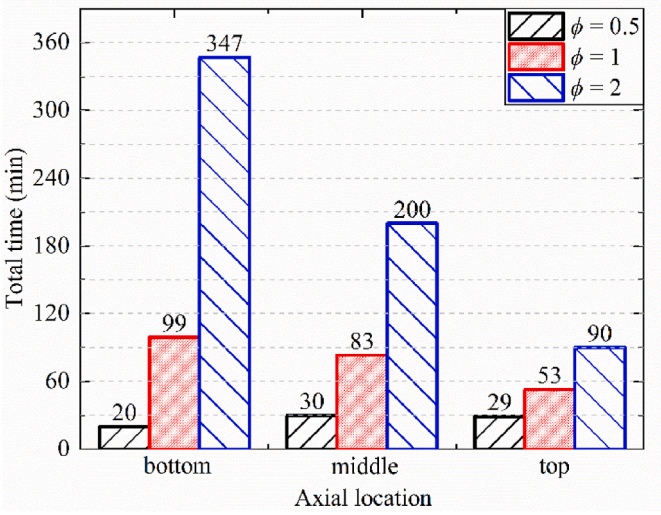

Fig. 16. Total time required for complete melting of H-PCM at different sections.

in complete melting time between bottom, middle and top sections increase significantly. For example, for the case of $\varphi = 1$, the time is 83 min and 53 min for middle and top sections, respectively, while for the case of $\varphi = 2$, the time is 200 min and 90 min for middle and top sections, respectively. This is mainly due to that the natural convection could have more time to take effect on the whole charging process, which would be further discussed shown below.

Fig. 17 shows the variation of local temperature of H-PCM with time. For the case of $\varphi = 0.5$, point A reaches the liquidus temperature in about 20 min, and then the temperature rises rapidly after absorbing sensible heat. For the case of $\varphi = 1$ & 2, the time for point A to reach the liquidus temperature is 100 min and 350 min, respectively. It is also clearly from Fig. 17(a) that the temperature in the case of $\varphi = 2$ remains at phase transition interval for much longer time, compared to other two cases. For point C in Fig. 17(b), the time used to reach the liquidus temperature is within 90 min for all cases, and the difference is much smaller than the ones of point A.

Fig. 18 shows the variation of maximum velocity of H-PCM zone with time. For the case of $\varphi = 0.5$, H-PCM velocity is less than 10 mm/s, and the duration of natural convection is very small (i.e. less than 40 min). Thus, the effect of natural convection on the whole melting process could be ignorable, which agrees well with the melting pattern shown in Fig. 16. With the increase of radius ratio, natural convection of H-PCM is

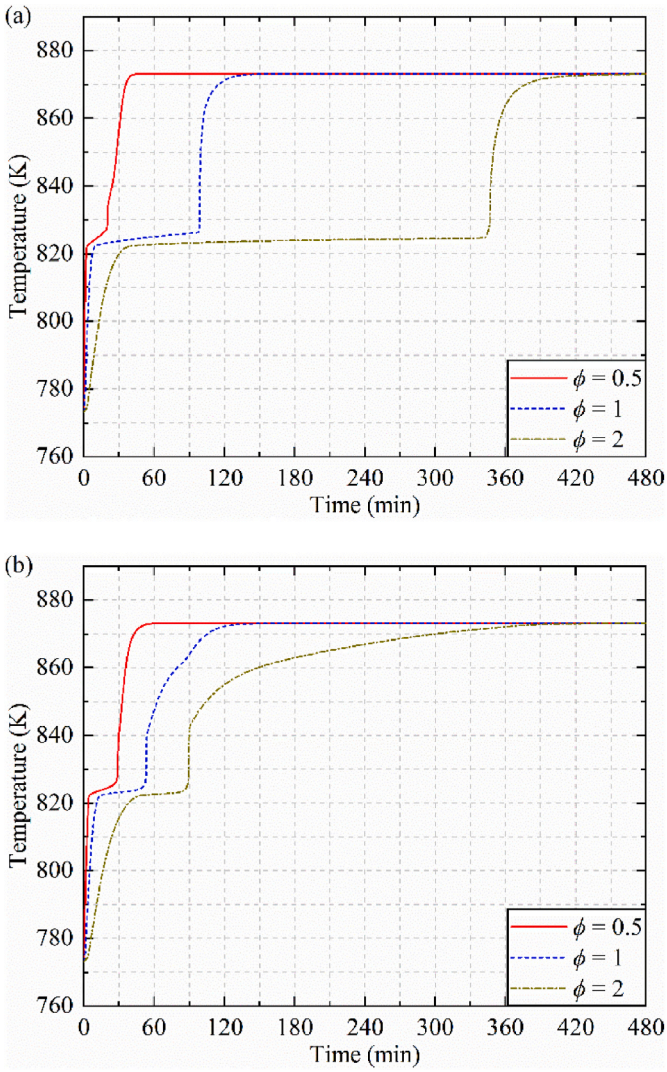

Fig. 17. Variation of local temperature of H-PCM with time: (a) point A at bottom section and (b) point C at top section.

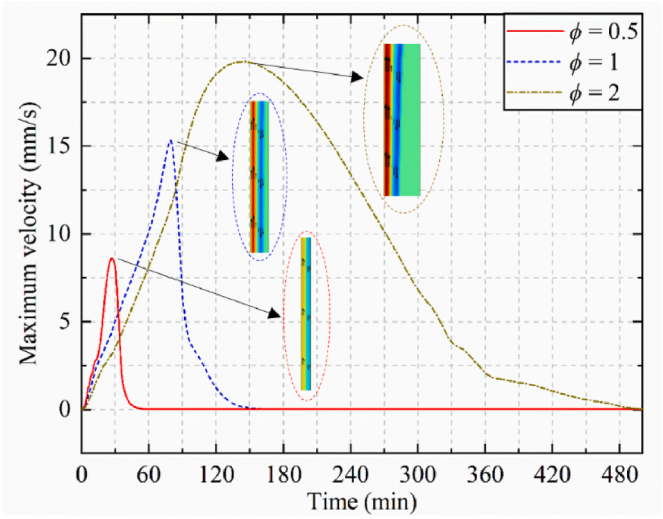

Fig. 18. Variation of maximum H-PCM velocity with time for the cases with different radius ratio φ.

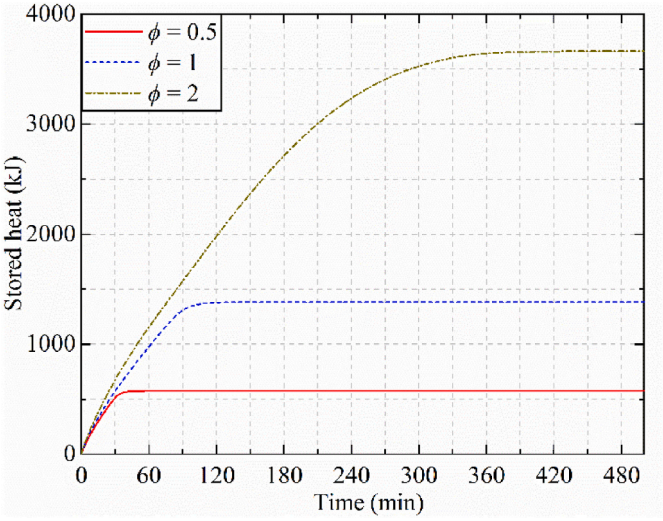

Fig. 19. Variation of stored heat of H-PCM with time for the cases with different radius ratio φ.

significantly enhanced, especially the duration of natural convection. For the case of $\varphi = 2$, the duration of natural convection is much longer while the maximum velocity could reach 20 mm/s. Thus, natural convection has an important effect on the whole melting process, i.e. temperature rising quickly at top section while remaining within the phase transition interval for a long time at bottom section, as shown in Fig. 17.

Fig. 19 shows the variation of the heat stored by the system in the charging process, for the case of φ is 0.5, the stored heat is about 575 kJ, which is finished in about 40 min. As the φ increases to 1 and 2, the stored heat increases to 1380 kJ in 120 min and 3650 kJ in 390 min, respectively. The amount of the increase of the stored heat is proportional to the volume of H-PCM. Although φ is different, the heat storage shows a trend of rapid increase at first and then gradually flattened. The heat storage rate also increases with the increase of φ. This is probably because the temperature difference between the H-PCM and S-CO_2 increases with the increase of φ during the same thermal storage time.

4. Conclusion

In this paper, a combined phase transition model is developed and validated against the data in literature. And the heat transfer between S-CO_2 and H-PCM in latent thermal storage system is investigated, where the effect of natural convection is focused, and the main results are summarised as follows:

1) The long duration of natural convection has a great influence on the melting process of H-PCM in the charging process. The melting pattern of H-PCM could be contrary between the cases with and without considering natural convection.
2) Compared to charging process, the velocity of H-PCM due to natural convection is much larger but the duration is quite short, resulting in little effect on the whole solidification process. It also suggests that duration of natural convection is more important than its maximum velocity.
3) With the increase of the initial temperature difference between S-CO_2 and H-PCM, the natural convection rate and energy release rate increase in the discharging process, but the melting pattern is not affected in both the charging and discharging processes.
4) For the case of small radius ratio, the effect of natural convection is ignorable. With the increase of the ratio between the S-CO_2 tube and H-PCM tank, the strength of the natural convection of melting H-PCM is enhanced, especially the duration of natural convection.

The results of this work are limited to the system with only one kind of H-PCM. The performance of the system could be improved by the cascaded H-PCM, which would be focused in future.

CRediT authorship contribution statement

Ming Zhu: Investigation, Writing – original draft. **Wenguang Nan:** Conceptualization, Investigation, Writing – original draft, Writing – review & editing. **Yueshe Wang:** Writing – review & editing.

Declaration of competing interest

The authors declare that they have no known competing financial interests or personal relationships that could have appeared to influence the work reported in this paper.

Acknowledgments

The support of National Natural Science Foundation of China (Grant No. 51806099) is gratefully acknowledged. The first author is grateful to Postgraduate Research & Practice Innovation Program of Jiangsu Province (College Project, JXSS-010) for the financial support of part of this work.

Appendix A

To examine the sensitivity of the simulation results to the grid size, three kinds of cells are used, i.e. 20 × 250 cells, 40 × 500 cells and 60 × 800 cells. The variation of local temperature of H-PCM with time is shown inFig. A1, where the point of (0.0128 m, 0.001 m) is used. For the simulation with 40 × 500 cells and more cells, the results are almost same. Therefore, 40 × 500 cells are used in Sections 3.1 and 3.2, and the same grid size is adopted in Section 3.3.

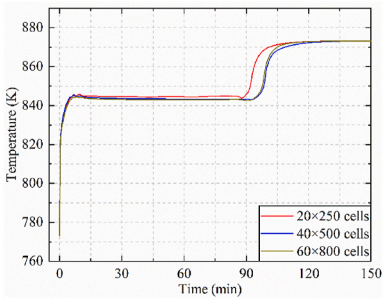

Fig. A1. Variation of local temperature of H-PCM with time in the simulations using different grid sizes.

References

[1] J. Rogelj, D. Huppmann, V. Krey, K. Riahi, L. Clarke, M. Gidden, Z. Nicholls, M. Meinshausen, A new scenario logic for the Paris Agreement long-term temperature goal, Nature 573 (2019) 357–363.

[2] E. Sala, J. Mayorga, D. Bradley, R.B. Cabral, et al., Protecting the global ocean for biodiversity, food and climate, Nature 592 (2021) 397–402.

[3] M. Salvia, D. Reckien, F. Pietrapertosa, et al., Will climate mitigation ambitions lead to carbon neutrality? An analysis of the local-level plans of 327 cities in the EU, Renew. Sust. Energy Rev. 135 (2021).

[4] J.M. Chen, Carbon neutrality: toward a sustainable future, Innovation 2 (2021), 100127.

[5] C. Smith, A.K. Hill, L. Torrente-Murciano, Current and future role of Haber–Bosch ammonia in a carbon-free energy landscape, Energy Environ. Sci. 13 (2020) 331–344.

[6] W. Aftab, A. Usman, J. Shi, K. Yuan, M. Qin, R. Zou, Phase change material-integrated latent heat storage systems for sustainable energy solutions, Energy Environ. Sci. 14 (2021) 4268–4291.

[7] C. Amy, H.R. Seyf, M.A. Steiner, D.J. Friedman, A. Henry, Thermal energy grid storage using multi-junction photovoltaics, Energy Environ. Sci. 12 (2019) 334–343.

[8] C. Ai, L. Zhang, W. Gao, G. Yang, D. Wu, L. Chen, W. Chen, A. Plummer, A review of energy storage technologies in hydraulic wind turbines, Energy Conv. Manag. (2022) 264.

[9] A.S. Virk, R. Shepherd, C. Park, Experimentally-validated numerical studies of thermal performance enhancement of latent thermal energy storage systems with periodically reciprocating flow, J. Energy Storage 55 (2022).

[10] X. He, J. Qiu, W. Wang, Y. Hou, M. Ayyub, Y. Shuai, A review on numerical simulation, optimization design and applications of packed-bed latent thermal energy storage system with spherical capsules, J. Energy Storage (2022) 51.

[11] Z. Li, Y. Lu, R. Huang, J. Chang, X. Yu, R. Jiang, X. Yu, A.P. Roskilly, Applications and technological challenges for heat recovery, storage and utilisation with latent thermal energy storage, Appl. Energy (2021) 283.

[12] N. Kumar, S.K. Gupta, Progress and application of phase change material in solar thermal energy: an overview, Mater. Today Proc. 44 (2021) 271–281.

[13] A.C. Caputo, A. Federici, P.M. Pelagagge, P. Salini, On the selection of design methodology for shell-and-tube heat exchangers optimization problems, Therm. Sci. Eng. Prog. 34 (2022).

[14] L.-Y. Chen, V.S.K. Adi, R. Laxmidewi, Shell and tube heat exchanger flexible design strategy for process operability, Case Stud. Therm. Eng. 37 (2022).

[15] J. Gasia, J. Diriken, M. Bourke, J. Van Bael, L.F. Cabeza, Comparative study of the thermal performance of four different shell-and-tube heat exchangers used as latent heat thermal energy storage systems, Renew. Energy 114 (2017) 934–944.

[16] S.S. Mostafavi Tehrani, Y. Shoraka, G. Diarce, R.A. Taylor, An improved, generalized effective thermal conductivity method for rapid design of high temperature shell-and-tube latent heat thermal energy storage systems, Renew. Energy 132 (2019) 694–708.

[17] D. Singh, W. Zhao, W. Yu, D.M. France, T. Kim, Analysis of a graphite foam–NaCl latent heat storage system for supercritical CO2 power cycles for concentrated solar power, Sol. Energy 118 (2015) 232–242.

[18] M. Liu, E.S. Omaraa, J. Qi, et al., Review and characterisation of high-temperature phase change material candidates between 500 C and 700°C, Renew. Sustain. Energy Rev. 150 (2021).

[19] S.S.M. Tehrani, R.A. Taylor, P. Saberi, G. Diarce, Design and feasibility of high temperature shell and tube latent heat thermal energy storage system for solar thermal power plants, Renew. Energy 96 (2016) 120–136.

[20] V. Tiwari, A.C. Rai, P. Srinivasan, Parametric analysis and optimization of a latent heat thermal energy storage system for concentrated solar power plants under realistic operating conditions, Renew. Energy 174 (2021) 305–319.

[21] T. Pirasaci, D.Y. Goswami, Influence of design on performance of a latent heat storage system for a direct steam generation power plant, Appl. Energy 162 (2016) 644–652.

[22] M. Liu, N.H.S. Tay, M. Belusko, F. Bruno, Investigation of cascaded shell and tube latent heat storage systems for solar tower power plants, Energy Proc. 69 (2015) 913–924.

[23] Y. Han, C. Zhang, Y. Zhu, X. Wu, T. Jin, J. Li, Investigation of heat transfer Exergy loss number and its application in optimization for the shell and helically coiled tube heat exchanger, Appl. Therm. Eng. (2022) 211.

[24] A. Erdogan, C.O. Colpan, D.M. Cakici, Thermal design and analysis of a shell and tube heat exchanger integrating a geothermal based organic Rankine cycle and parabolic trough solar collectors, Renew. Energy 109 (2017) 372–391.

[25] M. Pan, R. Smith, I. Bulatov, A novel optimization approach of improving energy recovery in retrofitting heat exchanger network with exchanger details, Energy 57 (2013) 188–200.

[26] J.M. Zamora, I.E. Grossmann, A comprehensive global optimization approach for thesynthesis of heat exchanger networks with no stream splits, Comput. Chem. Eng. 21 (1997) S65–S70.

[27] B. Cárdenas, N. León, High temperature latent heat thermal energy storage: phase change materials, design considerations and performance enhancement techniques, Renew. Sustain. Energy Rev. 27 (2013) 724–737.

[28] W. Zhao, Y. Zheng, J.C. Sabol, K. Tuzla, S. Neti, A. Oztekin, J.C. Chen, High temperature calorimetry and use of magnesium chloride for thermal energy storage, Renew. Energy 50 (2013) 988–993.

[29] M.R. Kadivar, M.A. Moghimi, P. Sapin, C.N. Markides, Annulus eccentricity optimisation of a phase-change material (PCM) horizontal double-pipe thermal energy store, J. Energy Storage 26 (2019).

[30] K. Nithyanandam, A. Barde, R.B. Lakeh, R.E. Wirz, Charge and discharge behavior of elemental sulfur in isochoric high temperature thermal energy storage systems, Appl. Energy 214 (2018) 166–177.

[31] S. Riahi, W.Y. Saman, F. Bruno, M. Belusko, N.H.S. Tay, Impact of periodic flow reversal of heat transfer fluid on the melting and solidification processes in a latent heat shell and tube storage system, Appl. Energy 191 (2017) 276–286.

[32] S. Riahi, W.Y. Saman, F. Bruno, M. Belusko, N.H.S. Tay, Comparative study of melting and solidification processes in different configurations of shell and tube high temperature latent heat storage system, Sol. Energy 150 (2017) 363–374.

[33] F. Fornarelli, S.M. Camporeale, B. Fortunato, et al., CFD analysis of melting process in a shell-and-tube latent heat storage for concentrated solar power plants, Appl. Energy 164 (2016) 711–722.

[34] S. Tiari, S. Qiu, M. Mahdavi, Numerical study of finned heat pipe-assisted thermal energy storage system with high temperature phase change material, Energy Convers. Manag. 89 (2015) 833–842.

[35] J. Sunku Prasad, P. Muthukumar, R. Anandalakshmi, H. Niyas, Comparative study of phase change phenomenon in high temperature cascade latent heat energy storage system using conduction and conduction-convection models, Sol. Energy 176 (2018) 627–637.

[36] C. Li, D. Chen, Y. Li, F. Li, R. Li, Q. Wu, X. Liu, J. Wei, S. He, B. Zhou, S. Allen, Exploring the interaction between renewables and energy storage for zero-carbon electricity systems, Energy (2022) 261.

[37] P. Wang, J. Wang, R. Jin, G. Li, M. Zhou, Q. Xia, Integrating biogas in regional energy systems to achieve near-zero carbon emissions, Appl. Energy (2022) 322.

[38] D.J. Arent, P. Green, Z. Abdullah, et al., Challenges and opportunities in decarbonizing the U.S. energy system, Renew. Sustain. Energy Rev. 169 (2022).

[39] D. Thanganadar, F. Fornarelli, S. Camporeale, F. Asfand, J. Gillard, K. Patchigolla, Thermo-economic analysis, optimisation and systematic integration of supercritical carbon dioxide cycle with sensible heat thermal energy storage for CSP application, Energy (2022) 238.

[40] R.Z. Huang Kaixin, Shengming Liao, Reserch on allowable flux density of supercritical CO2 solar receier, Acta Energ. Sol. Sin. 39 (2018) 44–50.

[41] H. Benoit, L. Spreafico, D. Gauthier, G. Flamant, Review of heat transfer fluids in tube-receivers used in concentrating solar thermal systems: properties and heat transfer coefficients, Renew. Sustain. Energy Rev. 55 (2016) 298–315.

[42] J. Liu, H. Chen, Y. Xu, L. Wang, C. Tan, A solar energy storage and power generation system based on supercritical carbon dioxide, Renew. Energy 64 (2014) 43–51.

[43] Z. Yang, L. Chen, Y. Li, Z. Xia, C. Wang, Numerical investigation of heat transfer characteristics in a shell-and-tube latent heat thermal energy storage system, Energy Proc. 160 (2019) 475–482.

[44] S. Seddegh, X. Wang, A.D. Henderson, Numerical investigation of heat transfer mechanism in a vertical shell and tube latent heat energy storage system, Appl. Therm. Eng. 87 (2015) 698–706.

[45] F. Rösler, D. Brüggemann, Shell-and-tube type latent heat thermal energy storage: numerical analysis and comparison with experiments, Heat Mass Tran. 47 (2011) 1027–1033.
[46] R.R. Kasibhatla, A. König-Haagen, F. Rösler, D. Brüggemann, Numerical modelling of melting and settling of an encapsulated PCM using variable viscosity, Heat Mass Tran. 53 (2016) 1735–1744.
[47] V.R. Voller, C. Prakash, A fixed grid numerical modelling methodology for convection-diffusion mushy region phase change problems, Int. J. Heat Mass Tran. 30 (1987) 1709–1719.
[48] O. Ben-David, A. Levy, B. Mikhailovich, A. Azulay, 3D numerical and experimental study of gallium melting in a rectangular container, Int. J. Heat Mass Tran. 67 (2013) 260–271.
[49] C. Gau, R. Viskanta, Melting and solidification of a pure metal on a vertical wall, J. Heat Tran. 108 (1986) 174–181.
[50] A.D. Brent, V.R. Voller, K.J. Reid, Enthalpy-porosity technique for modeling convection-diffusion phase change: application to the melting of a pure metal, Numer. Heat Tran. 13 (1988) 297–318.
[51] A. Trp, An experimental and numerical investigation of heat transfer during technical grade paraffin melting and solidification in a shell-and-tube latent thermal energy storage unit, Sol. Energy 79 (2005) 648–660.
[52] Y. Li, X. Xu, X. Wang, P. Li, Q. Hao, B. Xiao, Survey and evaluation of equations for thermophysical properties of binary/ternary eutectic salts from NaCl, KCl, MgCl2, CaCl2, ZnCl2 for heat transfer and thermal storage fluids in CSP, Sol. Energy 152 (2017) 57–79.
[53] K. Toerklep, H.A. Oeye, Viscosity of molten alkaline-earth chlorides, J. Chem. Eng. 27 (1982) 387–391.
[54] O. Takeda, Y. Hoshino, Y. Anbo, K.-i. Yanagase, M. Aono, Y. Sato, Viscosity of molten alkaline-earth fluorides, Int. J. Thermophys. 36 (2015) 648–657.